Journal of Thermal Analysis and Calorimetry (2020) 141:57–68
https://doi.org/10.1007/s10973-019-08901-6

On heat transfer and flow characteristics of jets impinging onto a concave surface with varying jet arrangements

Dandan Qiu[1] · Chenglong Wang[2] · Lei Luo[1] · Songtao Wang[1] · Zhiqi Zhao[1] · Zhongqi Wang[1]

Received: 12 June 2019 / Accepted: 5 October 2019 / Published online: 1 November 2019
© Akadémiai Kiadó, Budapest, Hungary 2019

Abstract

The increase in hot gas temperature is helpful for the turbine efficiency improvement and energy-saving. The significantly curved leading edge suffers the highest thermal load in a turbine blade. Jet impingement is one of the popular heat transfer enhancement methods, which has been widely used in blade leading edge. In this study, the flow structure and heat transfer characteristics of jets impinging onto a curved surface with varying jet arrangements and Reynolds number (10,000–40,000) are numerically investigated. The relative jet-to-target spacing equals 1, and relative surface curvature equals 10. An array jets arrangement is provided as baseline. Concerning three array cases, jet holes are positioned in inline and staggered patterns with changing jet-to-jet spacing. In this work, streamlines of different sections, limiting streamlines near target wall and vortex, are obtained. Local Nusselt number contour, local Nusselt number curves and surface-averaged Nusselt number are also presented. Local heat transfer characteristics are analyzed with fluid flow. It is also shown that the heat transfer uniformity of both inline and staggered cases is significantly enhanced by comparing with an array jets case. The whole curved surface-averaged Nusselt number increases with increasing jet-to-jet streamwise spacing at inline arrangement.

Keywords Heat transfer · Fluid flow · Jet impingement · Concave

List of symbols

d_{jet}	Jet diameter, mm
D	Target wall diameter, mm
D_1	Upper surface diameter, mm
f	Friction factor
f_s	Friction factor for an array jet
h	Heat transfer coefficient, W m^{-2} K^{-1}
l	Flow length, mm
L	Jet-to-jet spacing between middle and adjacent side jets at Y direction, mm
Nu	Nusselt number
Nu_{ave}	Averaged Nusselt number
$Nu_{ave,s}$	Averaged Nusselt number for an array jet
P	Jet-to-jet spacing for the same line jets at Y direction, mm
P_i	Inlet mass flow average total pressure, Pa
P_o	Outlet mass flow average total pressure, Pa
q	Heat flux, Wm^{-2}
Re	Jet Reynolds number
S	Streamwise direction along the concave target surface
T_i	Jet inlet temperature, K
T_w	Impingement wall temperature, K
U_i	Jet inlet velocity, m s^{-1}
Z	Jet-to-impingement surface spacing, mm
θ	Degree between the middle array jets and side arrays, °
λ	Fluid thermal conductivity, W m^{-1} K^{-1}
μ	Fluid dynamic viscosity, Pa s
ρ	Fluid density, kg m^{-3}

✉ Chenglong Wang
wangchenglonggfkd@163.com

[1] School of Energy Science and Engineering, Harbin Institute of Technology, Harbin 150001, China

[2] Science and Technology on Scramjet Laboratory, National University of Defense Technology, Changsha 410073, China

Introduction

The techniques employed to increase the turbine inlet temperature are conducive to improve the turbine efficiency and save the energy. Blade leading edge directly suffers from the high temperature of hot gas and becomes the highest thermal load portion of the blade due to such a severe working condition. Jet impingement is a common cooling method employed on the blade leading edge cooling for the

significant potential to increase the local heat transfer coefficient [1].

Some researchers investigated the fluid flow of single jet impinging onto a plane target at specified conditions. Sakakibara and Hishida [2] identified and clarified the vortical structure of a plane impinging jet with particle image velocimetry. Anderson and Longmire [3] measured the particle behavior in the stagnation zone and found that the particle motion in the stagnation zone was most depended on the mean flow. HadŽIabdiĆ and HanjaliĆ [4] performed large eddy simulations of jet impinging onto a plane with constant Re (jet Reynolds number) as 20,000 and jet-to-target spacing as 2. The results characterized the flow into some processes: tilting and breaking of the edge ring vortices before impinging, flapping, processing, splitting and pairing of stagnation point/ling, local unsteady separation and flow reversal at the onset of redial jet spreading, streak pairs and branching in the near-wall region of the radial jets. The heat transfer characteristics of jet impingement play an important role in the blade cooling design. Dairay et al. [5] focused on the effect of unsteady processes on the heat transfer coefficient with direct numerical simulation. The results inferred that the vertical distortions were responsible for the very high heat transfer zones. The investigation of varying jet and target parameters' effect on heat transfer characteristics for single jet impinging onto a flat plate was also researched. Lytle and Webb [6] and Volkov [7] revealed the effect of varying jet-to-plate distance on local heat transfer characteristics with experimental method and large eddy simulation, respectively. Attalla and Salem [8] presented the correlations of maximum and local Nusselt number as a function of Re, jet-to-plate inclination angle and jet-to-target spacing for specified three regions. Besides those mentioned above, the jet Reynolds number [9], jet fluid characteristics [10, 11], jet inlet profile [12] and target surface arrangement [10, 13] also play an important role in the heat transfer distributions.

In reality, applications such as multiple impingement jets are commonly used. And the fluid flow and heat transfer characteristics are mainly affected by the interactions between adjacent jets before they impinged on the target and surface flows depending on varying jet-to-jet spacing, jet arrangements and crossflow [14]. Behbahani [15] measured the local Nusselt number along span- and streamwise directions and area-averaged Nusselt number with varying Re (5000–15,000), jet-to-jet spacing (4, 8), jet-to-target distance (2–5) for 7 arrays with staggered plate jet impingement system. Hubber [16] reported the effects of jet-to-jet spacing (4, 6, 8), low nozzle-plate spacing (0.25, 1.0, 6.0) and Re (3500-20,400) on local- and area-averaged Nusselt number for 3*3 square arrays plate jets. Goodro [17–19] researched the local distributions and area-averaged Nusselt number of array jets impingement plate with varying Ma (Mach number), Re, temperature ratio, and proposed a new average Nusselt number correlation based on the works of Florschustz et al. [20]. San [21] reported the optimum jet-to-jet spacing for stagnation point Nusselt number of staggered plate jets impingement for specified Re (10,000–30,000), jet-to-jet spacing (4–16), jet-to-target distance (2–6). Xing [22] investigated the crossflow effect on both staggered and inline array jets with varying jet-to-target distance = 3, 4, 5. Yong [23] compared different jets' arrangement (staggered and inline) effect on plate Nusselt number of a semi-confined channel with varying Re (5000–25,000), jet-to-jet spacing (2–5), and jet-to-target distance (2–4).

These significant works introduced above are limited to plate jets impingement, which can be applied to the blade mid-cord cooling. However, the leading edge of a turbine blade is significantly curved (shown in Fig. 1 [20, 24]). The jets impingement characteristics are different on a curved impingement surface comparing with the plate case. Chupp et al. [25] experimentally measured the heat transfer effects of jet Reynolds number, dimensionless jet-to-target distance, jet-to-jet spacing and target surface curvature for an array of round jets impinging on a confined concave surface, and summarized the empirical correlations of stagnation point and area-averaged Nusselt number. Metzger [26] also reported correlations for maximum and local Stanton numbers for a row of circular jets impinging on a concave surface. Local Nusselt number distribution varying with different Re, jet-to-jet distance, jet-to-target distance, surface curvature was measured in the work of Bunker [27]. Kumar and Prasad [28] reported the computational results of the flow characteristics from an array of circular air jets impinging on a concave surface with varying Re (5000–67,800), inter-jet distance-to-jet diameter ratio (3.33, 4.67) and target plate distance-to-jet diameter ratio (1, 3, 4). Katti [29] measured the local pressure curves for an array jets impingement system with varying jet-to-jet distance, jet-to-target distance, surface curvature at 20,000 Re. Calzada [30] experimentally measured the Nusselt number distributions of two staggered array jets impinging onto the concave surface with varying Re by transient liquid crystal technique. More recently, the Nusselt number contours, pressure distributions and area-averaged Nusselt number correlations for an array jet were obtained by Patil

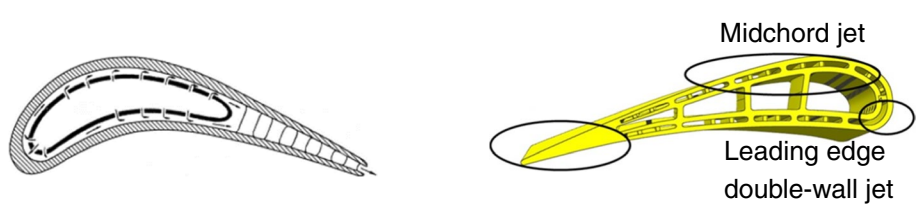

Fig. 1 Impingement cooling arrangement of typical gas turbine airfoil [17, 21]

[31] with varying Re (10,000–50,000), nozzle length (0.6, 1.0, 6.0), jet-to-target distance and surface curvature (3.33, 5.0, 10). Jung [32] conducted an experiment to investigate the effect of the injection angle for staggered three array impingement jets in a showerhead cooling system and compared with the following numerical results of fluid flow and heat transfer.

Even though similar works of the heat transfer augmentation in semi-cylindrical channels with single array or arrays jets can be found, most previous studies focused on the flow and geometry effects on averaged heat transfer or local heat transfer distributions. Very limited information is available for the relationship between flow structure and heat transfer. Concerning the averaged heat transfer parameters, most of the mean heat transfer parameters are averaged from the whole semi-cylinder range. In this study, jet arrangements' effect on the fluid flow and heat transfer characteristics of three array jets impinging onto a confined concave surface is numerically investigated at a constant jet-to-target spacing $Z/d_{jet} = 1$ and relative surface curvature $D/d_{jet} = 10$, where d_{jet} is the jet diameter. The jet Reynolds number is changing from 10,000 to 40,000. An array jets case is employed as the baseline. The characteristics of flow structure (vortex, streamlines, limiting streamlines), heat transfer and thermal performance for different cases are obtained. Local heat transfer characteristics are explained with the flow structures. To evaluate the heat transfer uniformity and enhancement region of different jets' arrangement cases, detailed comparisons between mean Nusselt numbers averaged from different surfaces (surfaces 1–3) of region are provided.

Problem description and boundary conditions

A three-dimensional, non-rotating, steady, compressible computation is conducted in this work. For a better understanding of the flow structure and heat transfer in blade leading edge, the internal cooling structure is simplified as a semi-cylinder double-wall channel. This channel is extended with a $12d_{jet}$ flat attachment at the tail zone to avoid reversed flow at the outlet for all cases. A sketch of the fluid model is presented in Fig. 2. All measurements presented are normalized by jet diameter d_{jet}. This investigation reveals the Reynolds number Re and jet arrangements' (inline, staggered) effects on the fluid flow and heat transfer characteristics of three array jets impinging onto a curved surface with constant jet-to-target spacing Z/d_{jet} and jet-to-jet spacing P/d_{jet}. For inline cases, the degree θ between the middle array jets and side arrays is changing from 25° to 45° (Fig. 2b). Concerning the staggered pattern, the distance L between the middle jets and adjacent side jet is $1.0d_{jet}$ and $2.0d_{jet}$ at Y direction. D_1 and D represent the diameter of upper and impingement surfaces, respectively. The details of the different cases are presented in Table 1. The baseline is an array jet placed at $\theta = 0°$ position with 4 d jet jet-to-jet spacing. The parameters in this study are set as $Z/d_{jet} = 1.0$, $D/d_{jet} = 10$, $P/d_{jet} = 4$, Re = 10,000–40,000 (Chupp et al. [25]), $\theta = 25°–45°$, $L/d_{jet} = 0, 1, 2$.

As shown in Fig. 2 b and d, surface 1 is the region of $\theta = -25°$ to 25°, $Y/d_{jet} = -2$ to 2; surface 2 is the region of $\theta = -45°$ to 45°, $Y/d_{jet} = -2$ to 2; and $\theta = -90°$ to 90°, $Y/d_{jet} = -2$ to 2 is set as the region of surface 3.

The no-slip, isothermal wall condition is applied to the target wall. The front and black surfaces are set as the periodic wall. The other surfaces are set as no-slip, adiabatic walls. The inlet flow employs the mass flow rate inlet and isothermal boundary condition at 5% turbulent intensity, and the outlet is a pressure outlet boundary. The temperature difference between inlet and impingement is 41 °C.

Computational solution method

Numerical simulations for the fluid flow and heat transfer of arrays jets impinging onto a concave surface have been conducted with the commercial solver FLUENT [33]. All predicted quantities were at steady state. The phase-coupled SIMPLE algorithm is used for the pressure–velocity coupling. Second-order accuracy is chosen for the discretization scheme for the convection terms of each governing equation. The computation is considered to be converged as the residual for the continuity equation, velocity, turbulence quantities was on the order of 1×10^{-5} and 1×10^{-7} for the energy equation.

Governing equations

The steady incompressible viscous fluid flow motion is governed by the equations below [34]:

Continuity equation

$$\frac{\partial\left(\rho\bar{u}_i\right)}{\partial x_i} = 0 \tag{1}$$

Momentum equation

$$\frac{\partial\left(\rho\bar{u}_i\bar{u}_j\right)}{\partial x_j} = -\frac{\partial\bar{P}}{\partial x_i} + \frac{\partial}{\partial x_j}\left(\left(\mu + \mu_t\right)\left(\frac{\partial\bar{u}_i}{\partial x_j} + \frac{\partial\bar{u}_j}{\partial x_i}\right)\right) \tag{2}$$

Energy equation for fluid

$$C_p\bar{u}_i\frac{\partial\rho\bar{T}}{\partial x_i} = \frac{\partial}{\partial x_i}\left(\lambda\frac{\partial\bar{T}}{\partial x_i}\right) - C_p\frac{\partial}{\partial x_i}\left(\frac{\mu_t}{\mathrm{Pr}_t}\frac{\partial\bar{T}}{\partial x_i}\right) \tag{3}$$

The computations were done by using RANS turbulence modeling combined with the $k\omega$-BSL turbulence model. The $k\omega$-BSL turbulence model is believed to improve the predictive capability for complex turbulent flows with flow swirling

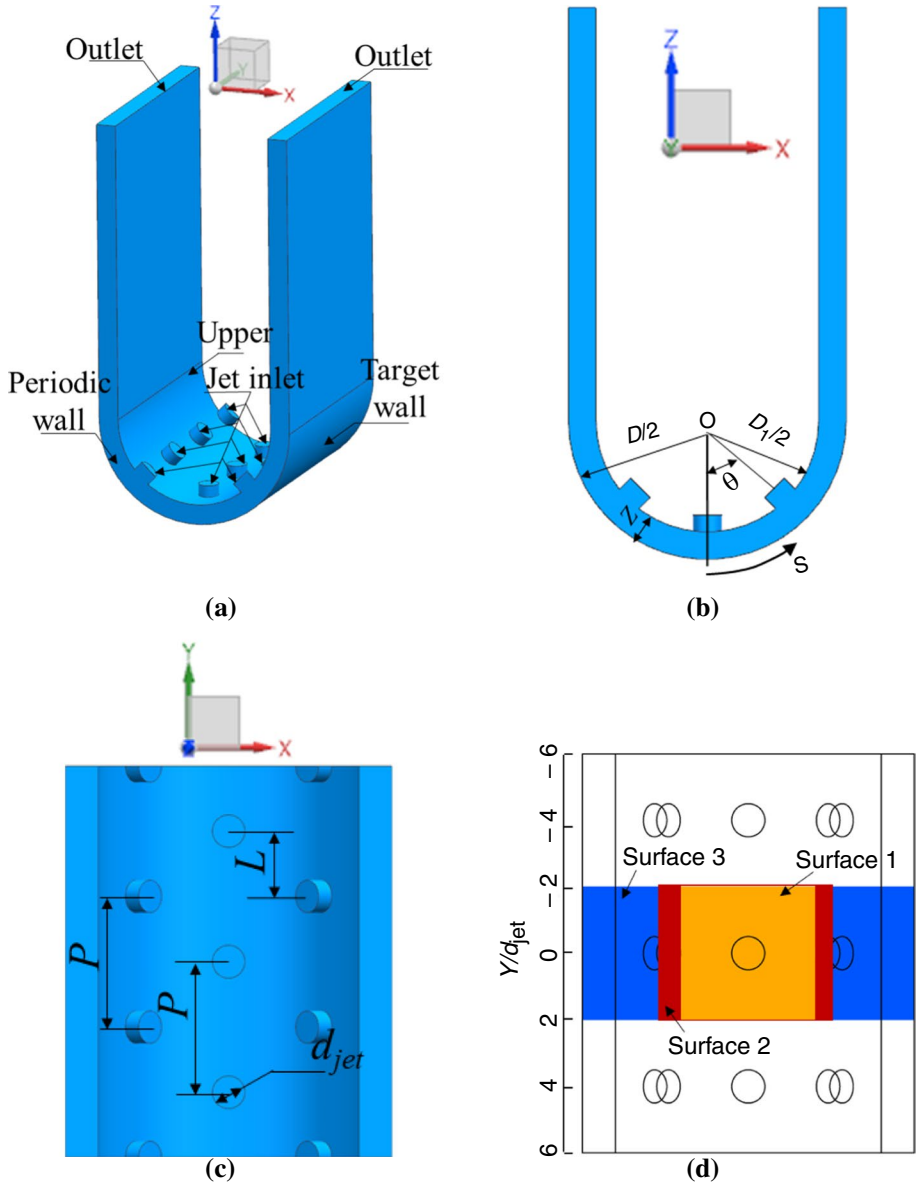

Fig. 2 A schematic picture (case 7) of the fluid flow model (**a**–**c**) and definition of surface 1, surface 2 and surface 3

Table 1 Cases' detailed information

Cases	Arrangement	P/d_{jet}	$\theta/°$	L/d_{jet}
Baseline	An array	4	–	–
Case 1	Inline	4	25	0
Case 2	Inline	4	30	0
Case 3	Inline	4	35	0
Case 4	Inline	4	40	0
Case 5	Inline	4	45	0
Case 6	Staggered	4	45	1.0
Case 7	Staggered	4	45	2.0

and separation, and it is also claimed to offer the best trade-off between accuracy and computational cost for the parameters considered [34–36]. Therefore, the $k\omega$-BSL turbulence model is employed, and the following equations are used.

The equation of the turbulent kinetic energy k reads

$$\frac{\partial(\rho k)}{\partial t} + \frac{\partial}{\partial x_i}(\rho k u_i) = \frac{\partial}{\partial x_i}\left[\left(\mu + \frac{\mu_t}{\sigma_{k3}}\right)\frac{\partial k}{\partial x_i}\right] + P_k - \beta^* \rho \omega k \tag{4}$$

The equation of the dissipation rate ω reads

$$\frac{\partial(\rho\omega)}{\partial t} + \frac{\partial}{\partial x_i}(\rho\omega u_i) = \frac{\partial}{\partial x_i}\left[\left(\mu + \frac{\mu_t}{\sigma_{\omega 3}}\right)\frac{\partial \omega}{\partial x_i}\right] + (1 - F_1)\frac{2\rho}{\sigma_{\omega 2}\omega}\frac{\partial k}{\partial x_i}\frac{\partial \omega}{\partial x_i} + \alpha_3 \frac{\omega}{k} P_k - \beta_3 \rho \omega^2 \tag{5}$$

where

$$\sigma_{k3} = F_1 \sigma_{k1} + (1 - F_1)\sigma_{k2} \tag{6}$$

$$\sigma_{\omega 3} = F_1\sigma_{\omega 1} + \left(1 - F_1\right)\sigma_{\omega 2} \tag{7}$$

$$\beta_3 = F_1\beta_1 + \left(1 - F_1\right)\beta_2 \tag{8}$$

$$\alpha_3 = F_1\alpha_1 + \left(1 - F_1\right)\alpha_2 \tag{9}$$

$$\mu_t = \rho\frac{k}{\omega} \tag{10}$$

$$P_{\mathrm{k}} = \mu_{\mathrm{t}}\left(\frac{\partial u_{\mathrm{i}}}{\partial x_{\mathrm{j}}} + \frac{\partial u_{\mathrm{j}}}{\partial x_{\mathrm{i}}}\right)\frac{\partial u_{\mathrm{i}}}{\partial x_{\mathrm{j}}} - \frac{2}{3}\frac{\partial u_{\mathrm{k}}}{\partial x_{\mathrm{k}}}\left(3\mu_t\frac{\partial u_{\mathrm{k}}}{\partial x_{\mathrm{k}}} + \rho k\right) \tag{11}$$

$$F_1 = \tanh\left(\arg_1^4\right) \tag{12}$$

$$\arg_1 = \min\left[\max\left(\frac{\sqrt{k}}{\beta^*\omega d}, \frac{500\nu}{d^2\omega}\right), \frac{4\rho\sigma_{\omega 2}k}{CD_{k\omega}d^2}\right] \tag{13}$$

$$\mathrm{CD}_{k\omega} = \max\left(\rho\sigma_{\omega 2}\frac{1}{\omega}\frac{\partial k}{\partial x_i}\frac{\partial w}{\partial x_i},\ 10^{-20}\right) \tag{14}$$

The constants have the values: $\sigma_{k1}=2, \sigma_{k2}=1, \sigma_{\omega 1}=2, \sigma_{\omega 2}=1/0.856, \beta_1 = 0.075, \beta_2 = 0.0828, \beta^* = 0.09,\ \alpha_1 = 5/9, \alpha_2 = 0.44, A_1=1.245, A_2=0, A_3=1.8, A_4=2.25, C_\mu=0.09$.

Mesh information

The structured mesh is generated by ICEM CFD [37] with the quality above 0.6 (shown in Fig. 3). Wall-resolved RANS grids with y+ < 1 are applied on walls. To ascertain the simulation accuracy and save computation costs, grid independence validation has been performed for an array case (the baseline) at Re = 20,000. Area-averaged Nusselt number on target surface and friction factor between jet inlet and $\theta = 90°$ section with changing mesh number is presented in Fig. 4. It is found that the averaged Nusselt number and friction factor are almost constant for 5.91 and 7.5 million grids. To get advantage of the computation time, the mesh configurations with 5.91 million elements are used for this work.

Data reduction

The Reynolds number is defined as:

$$\mathrm{Re} = \frac{\rho U_{\mathrm{i}} d_{\mathrm{jet}}}{\mu} \tag{15}$$

where U_{i} is the mean velocity at the inlet, d_{jet} is the hydraulic diameter of the jet inlet, and ρ and μ are the fluid density and dynamic viscosity, respectively.

The heat transfer coefficient h is defined as:

$$h = \frac{q}{T_{\mathrm{i}} - T_{\mathrm{w}}} \tag{16}$$

where q is the heat flux, T_{i} and T_{w} are considered as the temperature of the jet inlet and target surface, respectively.

The Nusselt number is defined as:

$$\mathrm{Nu} = h \times \frac{d_{\mathrm{jet}}}{\lambda} \tag{17}$$

where λ is the fluid thermal conductivity.

The friction factor is defined as:

$$f = \frac{P_{\mathrm{i}} - P_{\mathrm{o}}}{\frac{1}{2}\rho U_{\mathrm{i}}^2} \times \frac{d_{\mathrm{jet}}}{l} \tag{18}$$

where P_{i}, P_{o} are the mass flow average total pressures at inlet and $\theta = 25°$, 45°, 90° sections, respectively. l represents the relating flow length.

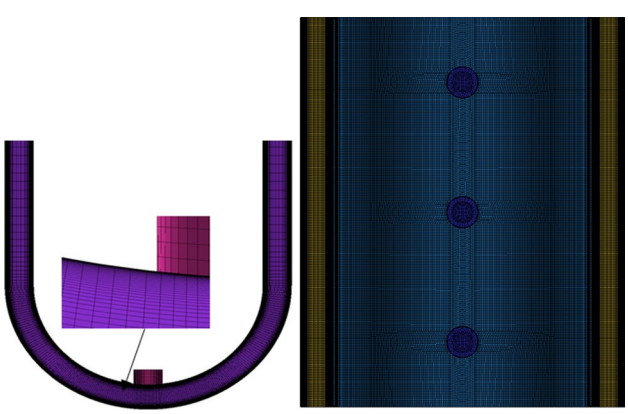

Fig. 3 Grid used in this study

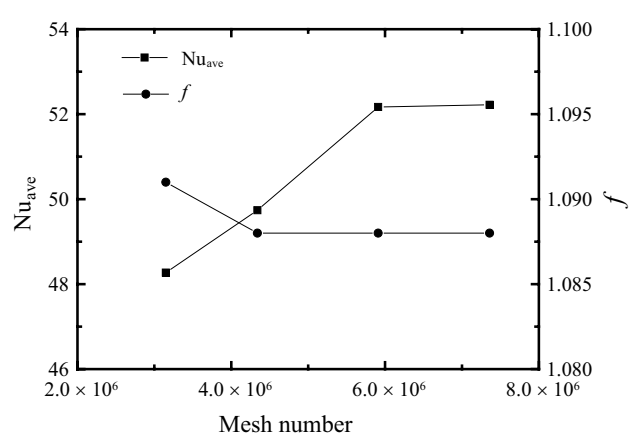

Fig. 4 Mesh independence study (baseline, Re = 20,000)

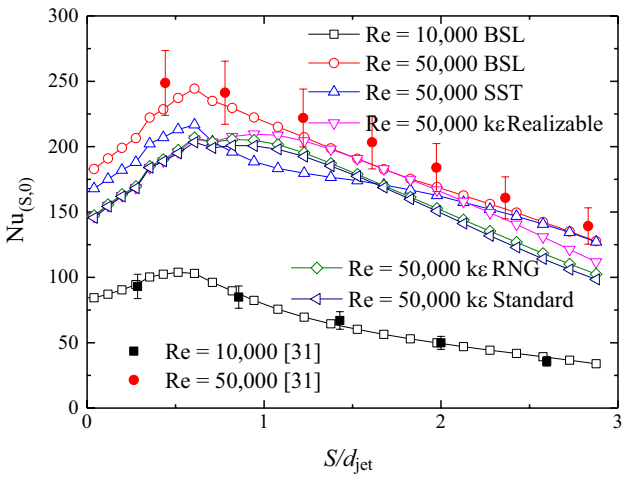

Fig. 5 Comparison of Nusselt number distributions in streamwise direction at $Y/d_{jet}=0$. The error bar is set as 10%

Table 2 Different included angle-averaged Nusselt number comparison between BSL turbulence model results and experiment work

		Nu_{ave} (surface 1)	Nu_{ave} (surface 2)
Re = 10,000	Patil [31]	205.68	160.67
	Present	200.26	151.93
	Difference	2.6%	5.4%
Re = 50,000	Patil [31]	73.78	56.71
	Present	79.48	56.63
	Difference	−7.7%	5.4%

CFD validations

In this study, the effort to verify the accuracy of the FLUENT simulations is conducted by comparing the streamwise local Nusselt number and area-averaged Nusselt number with the experiments of Patil [31]. The geometry in the literature (Patil [31]) is quite similar to that in the present work, and the case with $Z/d_{jet}=2$, $D/d_{jet}=10$, $P/d_{jet}=4$, Re = 10,000 and 50,000 is considered for comparison. As presented in Fig. 5, the simulations are carried out with several turbulence models available in FLUENT and the value of the Nusselt number is compared with the experimental data (Patil [31]). The error bar is set as 10% for experimental data which is the maximum uncertainty of the experiment. For Re = 50,000, the k-ε RNG and k-ε standard underpredicted the results significantly; the maximum inaccuracy is about 25%. The results of k-ω SST and k-ε realizable model are also much lower than the experiment for $S/d_{jet}<1$. It is found that the results for the BSL turbulence model followed the trends in the experiment for both Re = 10,000 and 50,000; the maximum inaccuracy is about 10% which is satisfied to the experiment maximum uncertainty. Table 2 also compares the averaged Nusselt number for different included angles, the maximum inaccuracy is lower than 10% and the BSL model is considered decently acceptable in the present work.

Results and discussion

Fluid flow and local heat transfer characteristics

In order to understand the fluid flow characteristics of jets impinging onto a confined concave surface, streamlines at different sections, limiting streamlines near the target wall and the vortex core between upper and target walls, are employed. The baseline, case 5 and case 7 at Re = 20,000 are introduced to discuss the relationship between fluid flow and heat transfer. Note that the mass flow rate of cases 5 and 7 is three times of baseline at the same Reynolds number. Due to the symmetry characteristics of the geometry and fluid flow, half part ($X/d_{jet}>0$) are presented for the near-wall surface limiting streamlines, vortex figures and Nusselt number plots.

Figure 6 provides the vortex core region with λ^2-criterion and streamlines at different sections of baseline case. Before the jets impinging onto the target wall, a pair of vortex (the main vortex pair, marked as A in Fig. 6a) occurs between adjacent jets, which can be related to the interaction of adjacent jets. This can be clearly observed at the sections' streamlines along streamwise direction. A pair of opposite recirculation (marked as a) can be observed between adjacent jets on $\theta=0°$, 25°, 30°, 35°, 40°, 45° sections (shown in Fig. 6b). Near $Y/d_{jet}=0$ of upper wall, surface vortex pair B can be found (Fig. 6a), and the relating recirculation pair b is also observed (Fig. 6b). This recirculation also occurs at $Y/d_{jet}=-4$, 4 of upper wall, which can be related to the interaction of upper surface and the adjacent branch of neighboring vortex pair A. As the heat transfer research object is the target wall, this paper will pay less attention to the fluid flow near the upper wall. Near the target wall, small vortex pair C occurs under the middle of vortex pair A. This can be attributed to the up-wash effect of two branches of vortex pair A and the restriction effect of target wall. From Fig. 6a, it is clear that the vortex pair C (at about $Y/d_{jet}=-2$) flows through recirculation pair of sections $\theta=0$, 40°. The relating region of recirculation pair (marked as c) is enlarging along streamwise direction (Fig. 6b).

Based on the flow characteristics of baseline mentioned above, the fluid flow of case 5 and case 7 is introduced. For the sake of comparison, streamlines on $\theta=0°$, 25°, 30°, 35°, 40°, 45° sections in $Y/d_{jet}=-2$–2 of baseline, case 5 and case 7 at Re = 20,000 are introduced in Fig. 7. As shown in Fig. 8, the vortex pair A is different from the baseline. Between the middle jet and side jet, the adjacent branches

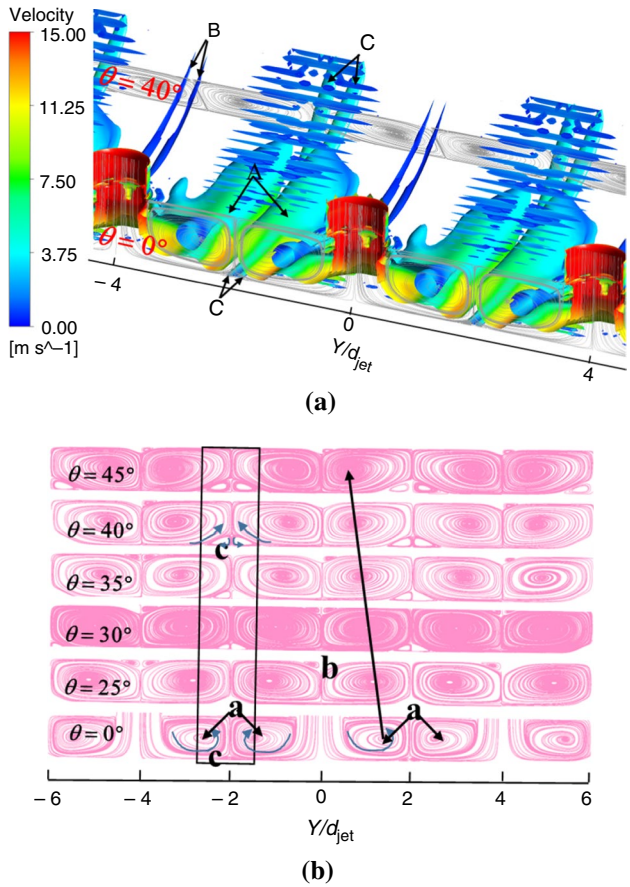

Fig. 6 Vortex and streamlines for baseline at Re = 20,000. **a** The vortex core region with λ^2-criterion and velocity colored for baseline at Re = 20,000 with streamlines on section $\theta = 0$, 45°; **b** streamlines on $\theta = 0°$, 25°, 30°, 35°, 40°, 45° sections

of vortex pair A gradually lift up from the target wall and approach to the $Y/d_{jet} = 0$ section. This behavior is clearly presented in the raising recirculation of streamlines pictures from sections $\theta = 0°$ to 35° (Fig. 7b). It is worth noting that two pairs of recirculation are found at streamline plots of section $\theta = 35°$. The inner one near $Y/d_{jet} = 0$ is induced by the adjacent branches of adjacent vortex pair A from middle jets. The outer one can be connected to vortex D. The generation of vortex D can be related to interaction of fluid flow from side and middle jets. Between the side and middle jets, two branches of flow from the side jet are twisted into one and flow around the side jet. Along streamwise direction, the twisted flow twins together with the flow from the side jet and moves to the outlet. Thus, vortex D occurs. As shown in Fig. 7b, the expanding recirculation (marked as d in Fig. 7b) of $\theta = 35°$ to 45° can be related to the movement of vortex D. Vortex pair C and recirculation pair c are also obtained. It can be inferred that the differences between case 5 and baseline can be mainly attributed to the interaction between fluid flow from middle jet and the side jet.

As presented in Figs. 7c and 9, the fluid flow characteristics are similar to case 5. Accompanying with the recirculation pair (a) moving up from target wall (see from section $\theta = 0°$–35°, Fig. 7c) and forward to $Y/d_{jet} = 0$ section, vortex pair A moves along the streamwise direction and lifts up with the interaction of side jets flow (Fig. 9). Vortex pair C, recirculation pair c, vortex D and recirculation pair d can also be observed.

Figure 10 illustrates the near target wall limiting streamlines of baseline, case 5 and case 7. For baseline, the reattachment line $R_{m,m}$ is obtained near the target wall at $Y/d_{jet} = 0$ (shown in Fig. 10a), which can be attributed to the interaction between the adjacent branches of adjacent vortex pairs A. As shown in Fig. 6b, the adjacent opposite recirculation of neighboring recirculation pairs (a) meets each

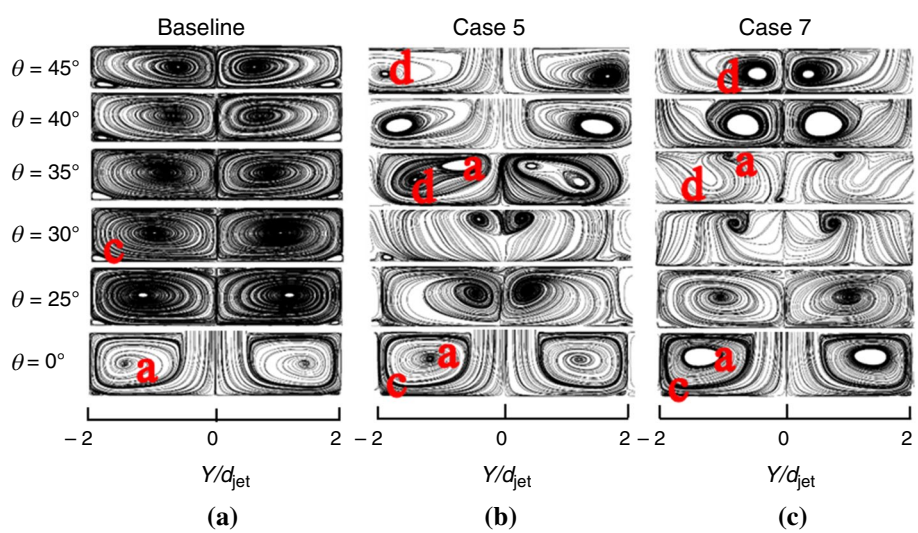

Fig. 7 Comparison of streamlines on $\theta = 0°$, 25°, 30°, 35°, 40°, 45° sections between baseline, case 5 and case 7 at Re = 20,000. **a** Streamlines for baseline, case 5 and case 7; **b** streamlines for case 5; **c** streamlines for case 7

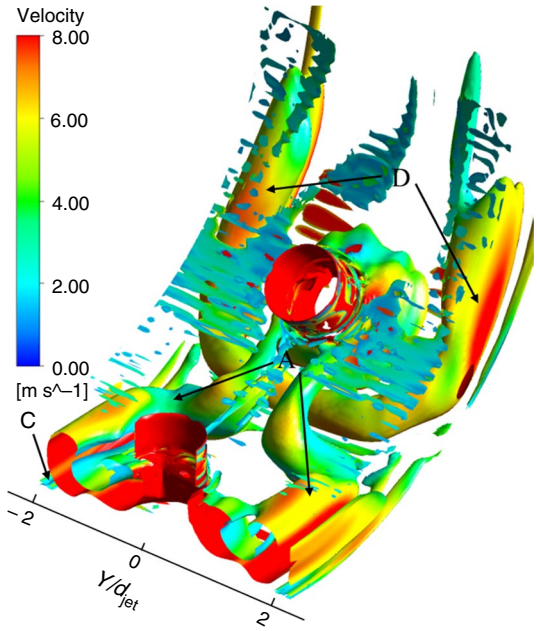

Fig. 8 The vortex core region with λ^2-criterion and velocity colored for case 5 at Re = 20,000

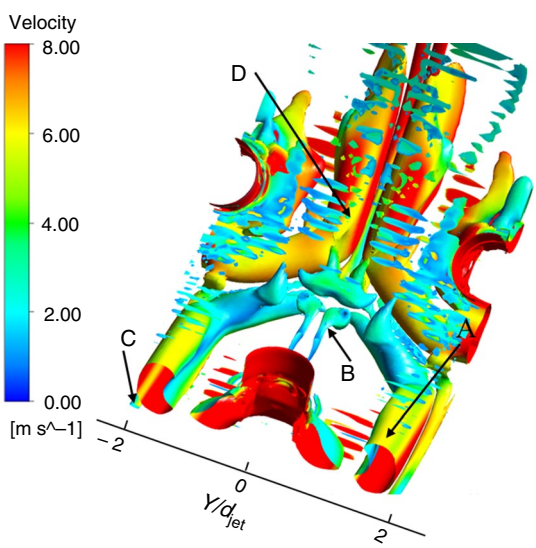

Fig. 9 The vortex core region with λ^2-criterion and velocity colored for case 7 at Re = 20,000

other at section $Y/d_{jet} = 0$, and fluid on this section reattaches onto the target wall; thus, the reattachment line $R_{m,m}$ occurs. Another reattachment line $R_{d,d}$ occurs near the target wall at $Y/d_{jet} = -2$ (shown in Fig. 10a), which can be related to the interaction of two branches of vortex pair C. The separation line $S_{d,m}$ (shown in Fig. 10a) can be related to the interaction between adjacent branches of vortex pairs A and C (section $\theta = 40°$, Fig. 6b). The enlarging part between $S_{d,m}$ and $R_{d,d}$ coincides with the enlarging recirculation c (blocked with black block in Fig. 6b) and vortex pair C (Fig. 6a) along streamwise direction. The decreasing area between $S_{d,m}$ and $R_{m,m}$ coincides with the closing behavior of adjacent recirculation of adjacent recirculation pairs a (Fig. 6b).

The limiting streamlines near target wall of case 5 are similar to baseline. As presented in Fig. 10b, reattachment lines $R_{m,m}$ and $R_{m,m2}$ of case 5 can be related to the interaction of the adjacent branches of adjacent vortex pairs A and two legs of vortex D, respectively. Reattachment line $R_{d,d}$ occurs and can also be attributed to the interaction of the two branches of vortex pair C. $R_{d,d2}$ may be related to near target wall vortex pair under adjacent vortex D. Separation line $S_{d,m}$ can be related to the interaction between adjacent branches of vortex A and C. The separation line S_2 moves along the movement path of vortex D. As shown in Fig. 10c, the attendance of reattachment lines $R_{m,m}$, $R_{m,m2}$, $R_{d,d}$ and $R_{d,d2}$ and separation line S_2 are similar to case 5. Another reattachment line R_2 between separation lines $S_{d,m}$ and S_2 can be observed.

Local Nusselt number distributions of baseline, case 5 and case 7 at Re = 20,000 are introduced in Fig. 11. Nusselt number distributions on $Y/d_{jet} = 0$, 1, 2 sections are presented in 12. For baseline (Fig. 11a), Nusselt number reaches the maximum value around the projection of jet hole and then decreases along the streamwise direction. At constant S/d_{jet}, Nusselt number is higher around $Y/d_{jet} = 0$. These can also be observed in Fig. 12a, the value of Nusselt number decreases after a peak occurs around $\theta = 7°$ at $Y/d_{jet} = 0$, higher value is obtained at $Y/d_{jet} = 0$ comparing with $Y/d_{jet} = 1$ position for constant S/d_{jet}, and the magnitude of Nusselt number for $Y/d_{jet} = 2$ is higher than $Y/d_{jet} = 1$. Those heat transfer characteristics discussed above can be related to the movement of vortex pairs. The decreasing Nusselt number along streamwise direction and higher value obtained around $Y/d_{jet} = 0$ at constant S/d_{jet} can be connected to the movement of the adjacent branches of vortex pair A, which gradually lift up and approach to $Y/d_{jet} = 0$ section along the streamwise direction. Between the adjacent jets (around $Y/d_{jet} = 2$), a relative high-strip region occurs coinciding with the location of vortex pair C (Fig. 6a) and $R_{m,m}$ (Fig. 10a) which can be related to the fluid reattachment. Comparing case 5 and case 7 with baseline (Fig. 11), the similar Nusselt number distributions can be observed. The maximum value occurs around the projection of jet hole, and a relative high-strip region presents between the adjacent jets at each line. The trends of Nusselt number distributions for $\theta < 15°$ and $\theta > 45°$ are similar to baseline of $\theta > 0°$ (Fig. 12). Concerning case 5, a small peak can be found around $\theta = 25°$ of $Y/d_{jet} = 0$, 1 (Fig. 12b) and can be related to the interaction between middle jet and side jets. For case 7, the distributions of Nusselt number at $\theta > 30°$ for section $Y/d_{jet} = 0$ are similar to case 5 at $Y/d_{jet} = 2$, and the trends for $Y/d_{jet} = 2$ are similar to case 5 at $Y/d_{jet} = 0$.

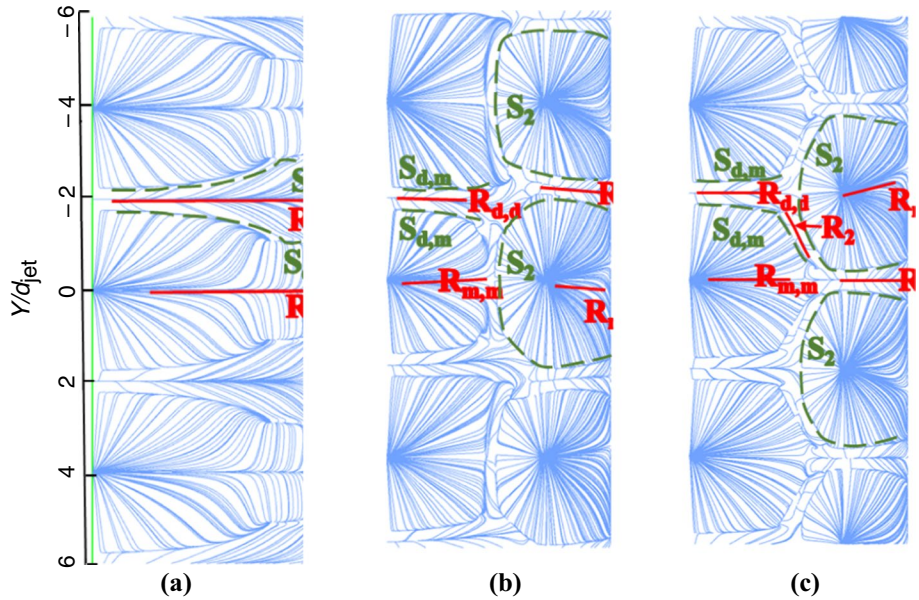

Fig. 10 Comparison of limiting streamlines near target wall at Re = 20,000. **a** baseline; **b** case 5; **c** case 7

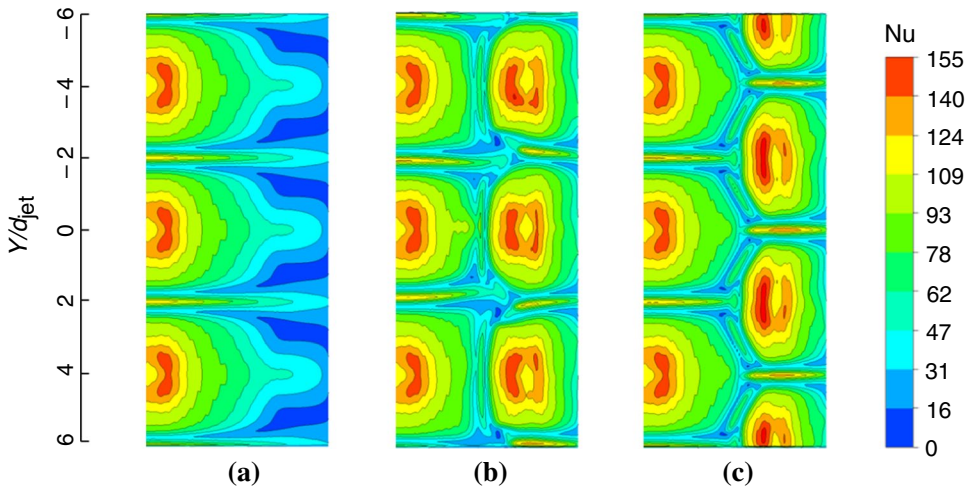

Fig. 11 Local Nusselt number distributions on target surface for baseline, case 5 and case 7 at Re = 20,000

Those can also be observed in Fig. 11b and c and can be related to the characteristics of staggered arrangement in case 7.

Overall discussion

Figure 13 illustrates the area-averaged Nusselt number for different cases and Re at surfaces 1–3. Generally, Re plays an unquestionable positive role in enhancing heat transfer for both inline and staggered arrangements. For cases 1–5, averaged Nusselt number for surface 1 shows a slight decrease from case 1 to case 2 and then increases from case 2 to case 5. Concerning surface 2 averaged Nusselt number, it increases slightly from case 1 to case 3 and decreases from case 3 to case 5. For surface 3 averaged value, Nu_{ave} increases as the side jets away from the middle (case 1 to case 5) as the side jets are arranged at staggered location of the middle jets (cases 6 and 7). Nu_{ave} of case 6 is a little lower than case 7 and case 5 for all surface-averaged situations. The Nusselt number averaged from surfaces 1–3 for case 7 is lightly higher than case 5 which coincides with the local distributions shown in Fig. 11. This can be related to the stronger flow disturbance for staggered arrangement.

The relative Nusselt number comparison between cases 1–7 at Re = 10,000, 30,000 is shown in Fig. 14; $Nu_{ave,s}$ is the value of baseline. At constant Re, the relative Nusselt numbers are about 1.2–1.35 and 1.4–1.62 for surface 2 and surface 3, respectively. As to the value of surface 1, $Nu_{ave}/Nu_{ave,s}$ is lower than 1, except the cases of case 5, case 7 at Re = 30,000 and case 1 at Re = 10,000. At small averaged surface (surface 1), cases 1, 5 and 7 perform better. As averaged surface enlarges (surface 2), inline

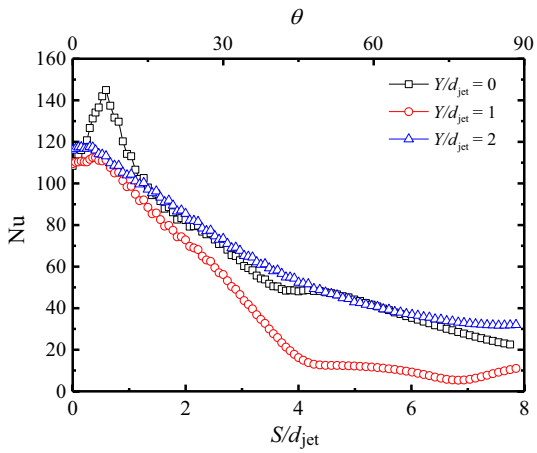

(a) Baseline

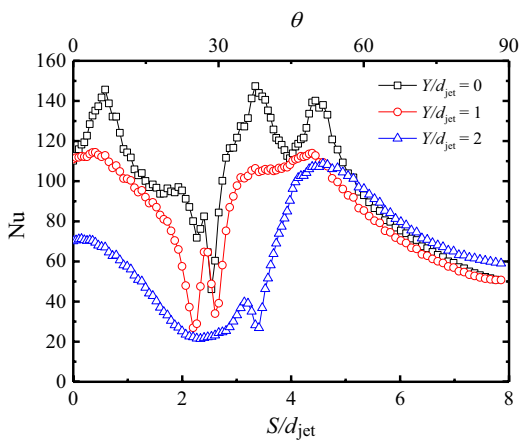

(b) Case 5

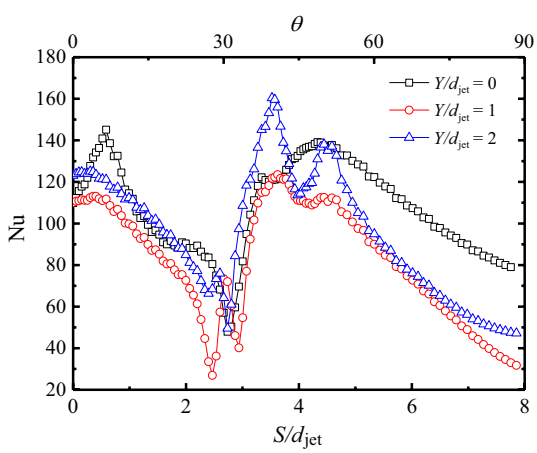

(c) Case 7

Fig. 12 Local Nusselt number curve at $Y/d_{jet} = 0$, 1, 2 for baseline (**a**), case 5 (**b**) and case 7 (**c**) at Re = 20,000

arrangement for side jets placed nearer to the middle jets (cases 1–4) reaches a relative high magnitude. For surface 3, values of case 5 and case 7 are higher. This may be attributed to the flow disturbance for different jet arrangements. As the side jets arranged farther from the middle

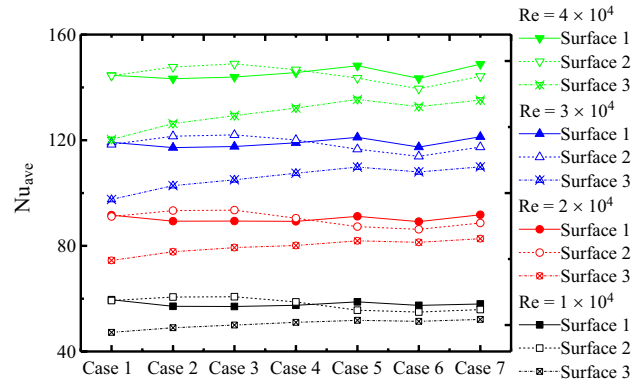

Fig. 13 Mean Nusselt number averaged from different surfaces at Re = 10,000–40,000 for cases 1–7

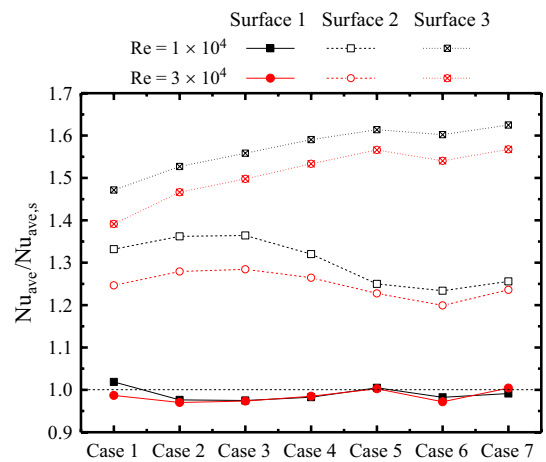

Fig. 14 Relative mean Nusselt number averaged from different surfaces for different cases at Re = 10,000 and 30,000 ($Nu_{ave,s}$ is the value of baseline)

jets (case 1 to 5), the disturbance effect of the side jets to the middle jets is weaker, and the flow disturbance near the outlet is stronger.

Figure 15 presents the Nusselt number ratio $Nu_{ave}/Nu_{ave,s}$ of cases 1–7 at constant inlet mass flow. Note that Nu_{ave} is the value of cases 1–7 at Re = 10,000, and $Nu_{ave,s}$ is the value of baseline at Re = 30,000. It is obvious that the relative Nusselt numbers are smaller than 1. From the view of surface-averaged Nusselt number, heat transfer enhancement is negative comparing with baseline. However, $Nu_{ave}/Nu_{ave,s}$ is increasing with an enlarging evaluated surface (surface 1 to surface 3); it can be inferred that the attendance of the side jets plays an effective role in the uniformity of heat transfer. For a large required cooling areas of blade leading edge, it may be better to change the single array jets into three array jets which can deduce the impingement force suffered by the thin blade leading edge and increase the uniformity of heat transfer. Among cases 1–7, the staggered arrangement

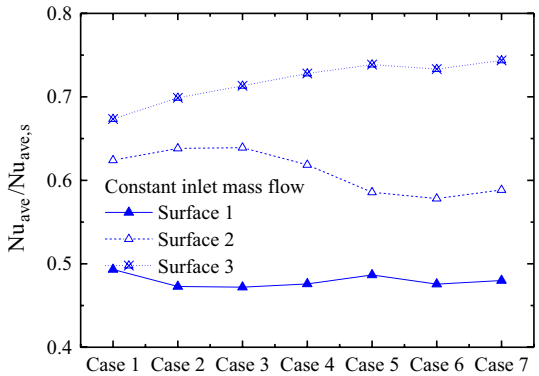

Fig. 15 Relative mean Nusselt number averaged from different surfaces for different cases at constant inlet mass flow (Nu_{ave} is the value of cases 1–7 at Re = 10,000; $Nu_{ave,s}$ is the value of baseline at Re = 30,000)

(case 7) reaches the highest value for surface 3, and inline situations at $\theta = 30°$ and 35° are better for surface 2.

Figure 16a provides a comparison of Nusselt number ratio with friction factor ratio between different cases. As shown in Fig. 16a, the dotted line $Nu_{ave}/Nu_{ave,s} = 1.0$ and dashed line $f/f_s = 1.0$ split this figure into four parts. At constant Re, the jet diameter-based Re is same for array jet cases and baseline (single-array jets case), and the values locate at region of $Nu_{ave}/Nu_{ave,s} > 1$, $f/f_s > 1.0$, except those for surface 1 averaged situation. For constant mass flow, the total inlet mass flow for cases 1–7 and baseline is same, surface 2 and surface 3 averaged values locate in $Nu_{ave}/Nu_{ave,s} < 1$, $f/f_s < 1.0$ region. The situation of $Nu_{ave}/Nu_{ave,s} < 1$, $f/f_s > 1.0$ for surface 1 averaged value of cases 2 and 3 performs bad heat transfer performance. It can be concluded that single-array jets impingent structure is more effectiveness to cool a small region of blade leading edge.

Figure 16b presents the $(Nu_{ave}/Nu_{ave,s})/(f/f_s)$ comparison of cases 1–7 for constant Re and mass flow conditions. The highest values of $(Nu_{ave}/Nu_{ave,s})/(f/f_s)$ for the same jets arrangement are almost produced by surface 3 averaged, and the lowest values are produced by surface 1 averaged. For cases 1–4, surface 2 and surface 3 averaged values are similar, and the differences between them increase for cases 5–7.

Conclusions

In this study, the three array jets' arrangement effect on the fluid flow and heat transfer characteristics is provided for a confined curved surface by numerical simulation. An array jets arrangement is introduced as the baseline. The detailed flow structures for an array and three array jets with inline and staggered arrangements are discussed. The local heat transfer characteristics are explained with the fluid flow

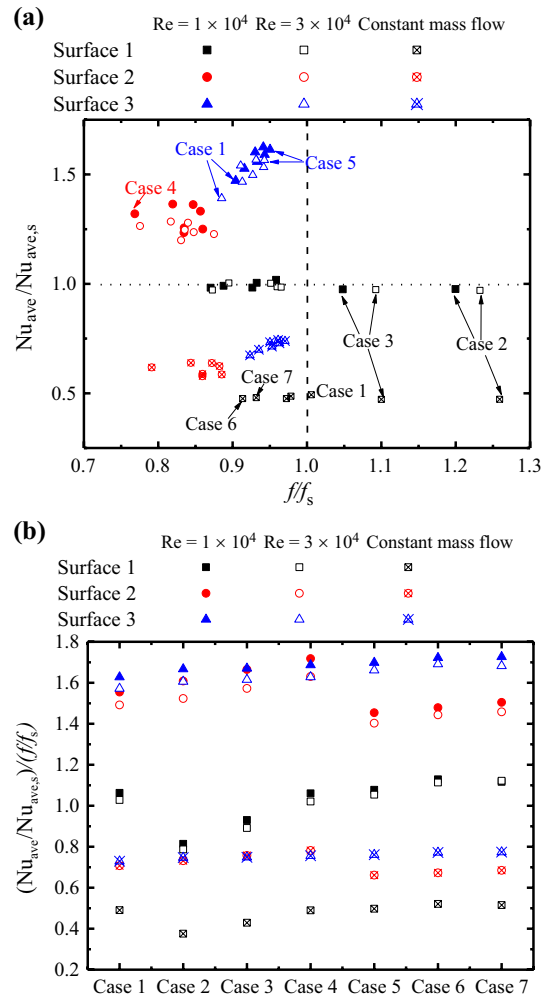

Fig. 16 Performance comparison

performance. The heat transfer uniformity is better as side array jets are located further to the middle array. The discussions about mean Nusselt number averaged from different surface area are helpful for the blade leading edge cooling design.

Acknowledgements The author acknowledges the financial support provided by the Natural Science Foundation of China (No. 51706051), China Postdoctoral Science Foundation funded Project (No. 2017M620116), Heilongjiang Postdoctoral Fund (No. LBH-Z17066) and the Fundamental Research Funds for the Central Universities (Grant No. HIT.NSRIF.2019061).

References

1. Han JC, Kwak JS. Heat transfer coefficients and film-cooling effectiveness on a gas turbine blade tip. ASME J Heat Transf. 2003;125(3):494–502.
2. Sakakibara J, Hishida K, Phillips WRC. On the vortical structure in a plane impinging jet. J Fluid Mech. 2001;434(434):273–300.

3. Anderson SL, Longmire EK. Particle motion in the stagnation zone of an impinging air jet. J Fluid Mech. 2006;299:333–66.
4. HadŽIabdiĆ M, HanjaliĆ K. Vortical structures and heat transfer in a round impinging jet. J Fluid Mech. 2008;596:221–60.
5. Dairay T, Fortuna V, Lamballais E. Direct numerical simulation of a turbulent jet impinging on a heated wall. J Fluid Mech. 2015;764:362–94.
6. Lytle D, Webb BW. Air jet impingement heat transfer at low nozzle-plate spacings. Int J Heat Mass Transf. 1994;37:1687–97.
7. Volkov KN. Interaction of a circular turbulent jet with a flat target. J Appl Mech Tech Phys. 2007;48(1):44–54.
8. Attalla M, Salem M. Heat transfer from a flat surface to an inclined impinging jet. Heat Mass Transf. 2014;50(7):915–22.
9. Agrawal C, Kumar R, Gupta A, Chatterjee B. Determination of rewetting velocity during jet impingement cooling of hot vertical rod. J Therm Anal Calorim. 2016;123(1):861–71.
10. Matheswaran MM, Arjunan TV, Somasundaram D. Analytical investigation of exergetic performance on jet impingement solar air heater with multiple arc protrusion obstacles. J Therm Anal Calorim. 2019;137(1):1–14.
11. Siavashi M, Rasam H, Izadi A. Similarity solution of air and nanofluid impingement cooling of a cylindrical porous heat sink. J Therm Anal Calorim. 2019;135(2):1399–415.
12. Tong AY. On the impingement heat transfer of an oblique free surface plane jet. Int J Heat Mass Transf. 2003;46(11):2077–85.
13. Xie Y. Flow and heat transfer characteristics of single jet impinging on dimpled surface. ASME J Heat Transf. 2013;135(5):052201.
14. Weigand B, Spring S. Multiple jet impingement a review. Heat Transf Res. 2011;42(2):101–42.
15. Behbahani AI, Goldstein RJ. Local heat transfer to staggered arrays of impinging circular air jets. ASME J Eng Gas Turbines Power. 1983;105(2):354–60.
16. Huber AM, Viskanta R. Effect of jet-jet spacing on convective heat transfer to confined impinging arrays of axisymmetric air jets. Int J Heat Mass Transf. 1994;37(18):2859–69.
17. Park J, Goodro M, Ligrani P, Fox M, Moon HK. Effects of mach number and Reynolds number on jet array impingement heat transfer. Int J Heat Mass Transf. 2007;50:367–80.
18. Goodro M, Park J, Ligrani P, Fox M, Moon HK. Effects of hole spacing on spatially-resolved jet array impingement heat transfer. Int J Heat Mass Transf. 2008;51:6243–53.
19. Goodro M, Park J, Ligrani P, Fox M, Moon HK. Effect of temperature ratio on jet array impingement heat transfer. ASME J Heat Transf. 2009;131(1):012201.
20. Florschuetz LW, Truman CR, Metzger DE. Streamwise flow and heat transfer distributions for jet array impingement with crossflow. ASME J Heat Transf. 1981;103:337–42.
21. San JY, Lai MD. Optimum Jet-to-jet spacing of heat transfer for staggered arrays of impinging air jets. Int J Heat Mass Transf. 2001;44:3997–4007.
22. Xing Y, Spring S, Weigand B. Experimental and numerical investigation of heat transfer characteristics of inline and staggered arrays of impinging jets. ASME J Heat Transf. 2010;132(9):53–8.
23. Shan Y, Zhang ZJ, Xie GN. Convective heat transfer for multiple rows of impinging air jets with small jet-to-jet spacing in a semi-confined channel. Int J Heat Mass Transf. 2015;86:832–42.
24. Luo L. On the design method and heat transfer mechanism of high efficiency cooling structure in a gas turbine. PhD thesis. China: Harbin Institute of Technology; 2016 (**in Chinese**).
25. Chupp RE, Helms HE, Mcfadden PW, Brown TR. Evaluation of internal heat-transfer coefficients for impingement-cooled turbine airfoils. J Aircr. 1969;6(3):203–8.
26. Metzger DE. Impingement cooling of concave surfaces with lines of circular air jets. ASME J Eng Gas Turbines Power. 1969;91(3):149–55.
27. Metzger DE, Bunker RS. Local heat transfer in internally cooled turbine airfoil leading edge regions: part i—impingement cooling without film coolant extraction. ASME J Turbomach. 1990;112(3):451–8.
28. Kumar BVNR, Prasad BVSSS. Computational flow and heat transfer of a row of circular jets impinging on a concave surface. Heat Mass Transf. 2007;44(6):667–78.
29. Katti V. Pressure distribution on a semi-circular concave surface impinged by a single row of circular jets. Exp Therm Fluid Sci. 2013;46:162–74.
30. Calzada PDL, Alvarez JJ. Experimental investigation on the heat transfer of a leading edge impingement cooling system for low pressure turbine vanes. ASME J Heat Transf. 2010;132(12):122202.
31. Patil VS, Vedula RP. Local heat transfer for jet impingement onto a concave surface including injection nozzle length to diameter and curvature ratio effects. Exp Therm Fluid Sci. 2018;92:375–89.
32. Jung EY, Chan UP, Dong HL, Kim KM, Cho HH. Effect of the injection angle on local heat transfer in a showerhead cooling with array impingement jets. Int J Therm Sci. 2018;124:344–55.
33. Fluent A. 12.0. Theory guide. 2009.
34. Versteeg H, Malalasekera W. An introduction to computational fluid dynamics: the finite volume method. 2nd ed. London: Pearson Education; 2007.
35. Menter FR. Two-equation eddy-viscosity turbulence models for engineering applications. AIAA J. 1994;32:1598–605.
36. Wallin S, Johansson A. A complete explicit algebraic reynolds stress model for incompressible and compressible flows. J Fluid Mech. 2000;403:89–132.
37. ANSYS ICEM CFD. 11.0 Help Manual. ANSYS Inc 2009.

Publisher's Note Springer Nature remains neutral with regard to jurisdictional claims in published maps and institutional affiliations.